International Journal of Heat and Mass Transfer 142 (2019) 118425

Contents lists available at ScienceDirect

International Journal of Heat and Mass Transfer

journal homepage: www.elsevier.com/locate/ijhmt

Heat flux evaluation in a multi-element CH_4/O_2 rocket combustor using an inverse heat transfer method

Nikolaos Perakis *, Julian Strauß, Oskar J. Haidn

Technical University of Munich, Chair of Turbomachinery and Flight Propulsion, Boltzmannstr. 15, 85748 Garching, Germany

ARTICLE INFO

Article history:
Received 11 December 2018
Received in revised form 6 May 2019
Accepted 15 July 2019

Keywords:
Inverse method
Rocket engine
Methane combustion
Heat transfer

ABSTRACT

Heat load measurements in experimental lab-scale rocket combustors are essential in order to obtain information about the mixing and energy release of the propellants, the injector/injector interaction as well as the injector/wall interaction. The present work demonstrates an efficient inverse method for estimating the spatially resolved heat flux distribution at the hot gas wall of multi-element, actively cooled engines using the information provided by temperature measurements in the material. This inverse method implements Nusselt-correlations for the estimation of the wall heat transfer coefficient in the cooling channels and a Jacobi-matrix based optimization algorithm for the calculation of the hot gas side heat flux. The method is applied for the evaluation of CH_4/O_2 test data. A water-cooled 7-injector rocket combustor is investigated, which is operated at the Chair of Turbomachinery and Flight Propulsion (LTF) of the Technical University of Munich (TUM). The use of the inverse method gives significant information about the axial and azimuthal distribution of the heat flux. The azimuthal distribution sheds light into the interaction between the individual flames. Specifically, the angular position of maximal heat flux appears to shift from directly above the injector elements towards the positions between two neighboring elements, implying the presence of a strong vortex system pushing hot gas directly onto the wall. The obtained results agree qualitatively with RANS simulations of the hot gas flow.

1. Introduction

In an effort to decrease launch costs and to produce reliable and efficient propulsion devices for space applications, significant research efforts have been placed in advancing the maturity level of the propellant combination methane/oxygen. Within the past decades many space-faring nations have investigated and developed technologies for liquid propellant rocket engines operating with methane/oxygen. NASA has successfully developed and tested a prototype planetary lander propelled by a LOX/LCH_4 20kN class engine within the Morpheus project [1,2], whereas in Europe a low cost LOX/LCH_4 engine prototype named Prometheus is scheduled [3] with the purpose of powering the next generation of launchers after Ariane 6. The collaboration of industry and space agencies in Europe is manifested in the development of the LM-10 MIRA engine for the upper stage of the VEGA-E launcher [4] and the ACE-42R reusable engine for a space plane concept. The interest of private companies in the LOX/LCH_4 propellant is also evident from the development of the BE-4 and Raptor engines, which will power the Vulcan and ITS launch vehicles respectively [5]. Finally, South Korea is also looking into advancing the status of methane/oxygen engines [6], whereas in Japan the LE-8 engine, as well as a 30 kN- and a 100 kN-class engine have been successfully tested [7,8].

The reasons for the increased research interest in methane/oxygen are mainly the fact that it combines great performance with reusability and sustainability. Apart from the high specific impulse (highest among hydrocarbons) and the large density which leads to small tank volumes [9], the large boiling temperature compared to hydrogen allows for less demanding cooling and thermal insulation of the tanks to minimize vaporization and heat-exchange with the oxygen tank. Reusability is achieved by the low coking-rate of methane under the thermal conditions typical for cooling channels [10] and the lower thermal strain induced to the engine structure due to the temperature difference of coolant and hot gas compared to hydrogen engines [11]. Sustainability is ensured by the existence of various methods for obtaining bio-methane and the methods for renewable natural gas production [12,13]. Finally, the costs can be further reduced by substituting the costly helium with nitrogen for the pressurization of the tanks.

* Corresponding author.
E-mail address: nikolaos.perakis@tum.de (N. Perakis).

https://doi.org/10.1016/j.ijheatmasstransfer.2019.07.075
0017-9310/

Nomenclature

c^*	characteristic velocity [m/s]
c_p	specific heat capacity [J/(kg · K)]
d	diameter [m]
h	heat transfer coefficient [W/(m^2 · K)]
J	residual function [K^2]
k	iteration index [–]
$\dot{m}$	mass flow rate [kg/s]
M	number of thermocouples [–]
N	number of parameter points [–]
$\mathbf{n}$	outwards pointing normal direction [m]
Nu	Nusselt number [–]
p	chamber pressure [bar]
Pr	Prandtl number [–]
r	radius [m]
$\dot{q}$	heat flux [W/m^2]
Re	Reynolds number [–]
$\mathbf{S}$	Jacobi matrix [K · m^2/W]
T	temperature [K]
x	axial coordinate [m]
ε	residual convergence limit [K^2]
ϵ	error [%]
θ	circumferential coordinate [°]
λ	thermal conductivity [W/(m · K)]
μ	dynamic viscosity [Pa · s]

Subscripts

0	reference
acc	accuracy
c	calculated
cc	cooling channel
corr	correlation
fu	fuel
inj	injector
loc	location
m	measured
mat	material
ox	oxidizer
prec	precision
tot	total
w	wall

In order to better understand the characteristics of this promising propellant combination, the design and testing of sub-scale engines is required. Specifically, before the design of full-scale engines, tests using single-element and multi-element sub-scale hardware are performed [7,8,14,15]. The knowledge about the performance of the injector elements, i.e. the mixing of the propellants, the injector/injector interaction and injector/wall interaction in the sub-scale experiments is used as an input for the improvement of the full-scale design without the need for costly full-scale testing.

The test data obtained from the sub-scale configurations are also used to provide validation data for numerical simulations. The necessity for a reliable prediction of the combustion characteristics and the heat loads within a combustion chamber and nozzle has promoted computational fluid dynamics (CFD) to become an integral part of the design process in the space propulsion industry. Apart from the prediction of performance merits such as the specific impulse and the characteristic velocity c^*, the calculated pressure profiles along the axial position $p(x)$ as well as the heat flux values at the hot gas wall $\dot{q}(x)$ are compared to the available experimental data. The need for this data over a wide range of operational conditions is even more critical for the innovative propellant combination of methane/oxygen due to the limited number of available tests [16–20].

Of the previously mentioned quantities, the one having the largest significance for the understanding of the physical and chemical phenomena is the heat flux. Due to the harsh environment within the chamber hot gas, the installation of sensors measuring gas temperature is almost impossible. Given the limited access to the burning gas, the heat flux distributions are usually utilized to deduce information about the conditions within the chamber. Moreover the prediction of the engine's lifetime, the design of an effective cooling system and the reliability of the chamber components after a specific number of tests is imminently connected to the heat loads applied onto the chamber wall thereby increasing the importance of this quantity even more.

The calculation of the average heat flux in experiments with active cooling system is easily carried out by means of the calorimetric method. However, the axial resolution of this method is restricted since it is defined by the number of cooling segments present in the hardware. Moreover, obtaining information about the azimuthal distribution becomes challenging and is usually not an option since the inlet and outlet temperature is measured in mixing manifolds [20]. Using temperature readings within the chamber material however, a reconstruction of the axially and azimuthally resolved heat flux profiles is possible. This method requires the solution of an inverse problem. The problem is considered to be an "inverse" one, since the causes (heat flux) that lead to a measured effect (temperature at specific locations) are sought.

Of particular interest are heat flux data for multi-element sub-scale engines due to the additional complexity introduced in the presence of flame-flame interaction. The interaction of the individual injectors leads to a local variation of the wall heat flux along the azimuthal direction, a phenomenon which is representative for full-scale hardware as well [21]. Extensive studies of wall heat flux evaluation in multi-element configurations with the purpose of resolving the azimuthal distributions are however limited. Conjugated heat transfer simulations of combustion and heat transfer in sub-scale and full-scale engines by Negishi et al. [22,23], Song et al. [24] as well as Daimon et al. [25] have demonstrated that the local heat flux values can significantly be increased by the secondary flow structures induced by the interaction of the individual flames. Similar results have been reported in experimental studies by Suslov et al. [26].

The present work introduces an inverse method for the evaluation of the heat loads in actively cooled rocket engines. The method can be applied to the evaluation of axially and circumferentially varying heat loads in multi-element sub-scale and full-scale rocket thrust chambers without a large computational cost. The main attributes of the method are the use of a Newton-Raphson optimization method and the approximation of the wall heat transfer in the cooling channels with a Nusselt-correlation. The method is applied for the evaluation of the heat loads in a GOX/GCH$_4$ multi-element chamber. Information about the flow-field, heat release and injector/injector interaction can be deduced from the resulting heat flux values and compared to existing CFD results.

In Section 2 a description of the chosen hardware is presented, whereas in Section 3 the properties of the inverse method are outlined in detail. The error analysis in Section 4 aims to quantify the uncertainties of the heat flux and temperature evaluation. The results of the inverse method as well as the comparison with the calorimetric method and previous CFD results is given in Section 5.

2. Experimental setup

The inverse heat conduction method presented in this work was initially developed with the purpose of evaluating the experimental heat flux stemming from the hot runs of capacitively and actively cooled rocket combustors operated at the Space Propulsion Division (RFA) of the Technical University of Munich (TUM). Within the framework of the German National Science Foundation (DFG) the DFG-TRR40 project entitled "Fundamental Technologies for the Development of Future Space-Transport-System Components under High Thermal and Mechanical Loads" has been funded, aiming at increasing the experience around the propellant combination methane/oxygen for future space applications [15].

In particular, the Space Propulsion Division of TUM has been working with these propellants for the past years employing different model combustors to provide detailed data about injector/injector and injector/wall interaction both for furthering identification and quantification of key phenomena and processes and for validation of engineering design tools [27,28]. For an optimum cooling system and specifically the cooling channel design, it is essential to know in sufficient detail the axial and azimuthal heat load distributions for a particular injector geometry and their sensitivity towards variations of the operating condition.

The examined multi-injector combustion chamber was designed for GOX and GCH_4 allowing high chamber pressures (up to 100 bar) and film cooling behavior examination. One of the key aspects of the project is to improve the knowledge on heat transfer processes and cooling methods in the combustion chamber, which is mandatory for the engine design. The attention is focused, in particular, on injector-injector and injector-wall interaction. In order to have a first characterization of the injectors' behavior, the multi-element combustion chamber is tested at low combustion chamber pressures and for a wide range of mixture ratios [29].

The seven-element rocket combustion chamber has an inner diameter of 30 mm and a contraction ratio of 2.5 in order to achieve Mach numbers similar to the ones in most rocket engine applications. The combustion chamber, depicted in Fig. 1, consists of four cylindrical water cooled chamber segments, as well as a nozzle segment (individually cooled), adding up to a total length of 382 mm. For the current study, shear coaxial injector elements are integrated. The test configuration includes the GOX post being mounted flush with respect to the injection face. The geometry of the injector is described in Table 1 and shown in Fig. 2.

In the present work, operating points with mean combustion chamber pressure of 20 and 30 bar and mixture ratios between 2.6 and 3.4 are chosen. The experimental data made available for the numerical evaluation include the mass flow rates of water at the inlet, the water pressure, the wall temperature at distinct locations and the integral heat flux values. For the determination of the heat flux values in the four chamber segments (A-D) and the nozzle (N), a calorimetric method is applied. The average heat flux of each chamber segment is determined by the enthalpy difference of the coolant between inlet and outlet. This is obtained by precise temperature measurements in the water manifolds between the test segments. Two separate cooling cycles are implemented: one for the first four segments in the combustion chamber and an additional cooling cycle for the nozzle segment, both in co-flow configuration with the hot gas. As described in Section 3, the present study focuses on chamber segment A, in which the cooling channels have a rectangular cross section. The geometry of the cooling channels and the operating conditions for the coolant in the first chamber segment are summarized in Table 2.

The wall temperature values available as inputs for the inverse method are obtained at radial distances of 0.7–1.5 mm from the hot gas wall. Each of the 8 axial positions equipped with thermocouples, alternates between 0.7 and 1.5 mm, with the first location at 2.5 mm downstream of the injector having a hot gas wall distance of 1.5 mm. Type T thermocouples with 0.5 mm diameter are installed to measure the temperature within the structure.

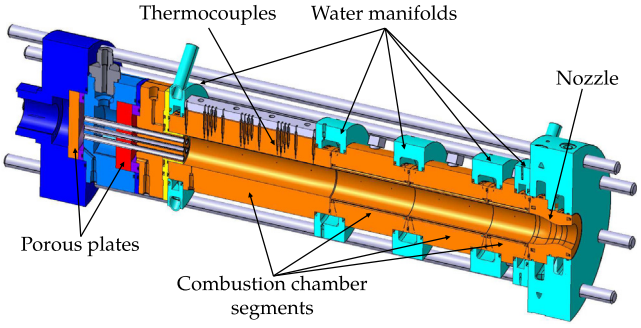

Fig. 1. Sketch of the combustion chamber.

Table 1
Summary of injector dimensions.

Dimension	Value
Oxygen port diameter d_{ox}	4.0 mm
Methane annulus inner diameter $d_{fu,in}$	5.0 mm
Methane annulus outer diameter $d_{fu,out}$	6.0 mm
Distance between injector centers $d_{inj,inj}$	9.0 mm
Distance between injector center and wall $d_{inj,wall}$	6.0 mm

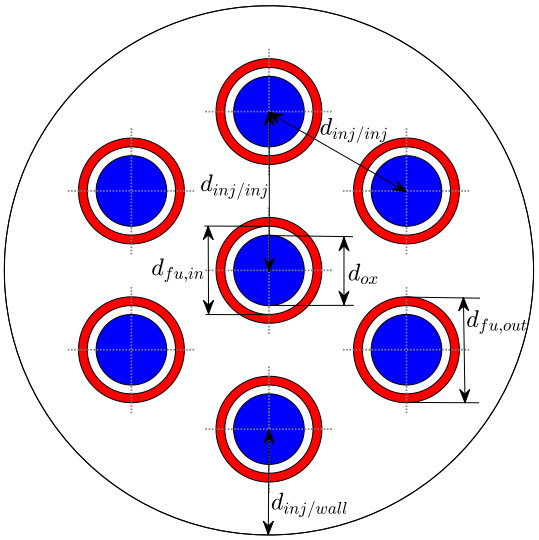

Fig. 2. Sketch of the injector faceplate.

Table 2
Summary of cooling channels geometry and operating point.

Dimension	Value
Cooling channel height	3.5 mm
Cooling channel width	1.5 mm
Aspect ratio	2.33
Distance of cooling channel to hot gas wall	1.5 mm
Mass flow rate (per channel)	13.89 g/s
Inlet pressure	40 bar
Inlet temperature segment A	285.0 K
Outlet temperature segment A	304.5 K
Reynolds number	5550

The locations of the thermocouples relative to the cooling channels are shown in the right sub-figure of Fig. 6. The inner part of the chamber (until the radius corresponding to the end of the cooling channels) consists of a CuCrZr alloy, whereas the outer part has been manufactured using copper electroplating.

3. Inverse heat transfer method

Experimental lab-scale rocket combustors cooled by a water cycle or other cooling medium have the characteristic property of reaching a steady state temperature distribution after the first seconds of operation. This effect is utilized when evaluating the heat flux profiles, since the latter ones can simply be obtained from the enthalpy difference of the outgoing and incoming coolant flow. The calorimetric method however only provides average values and its resolution is given by the number of cooling segments. For a more detailed distribution, the temperature field has to be reconstructed using an inverse method.

Inverse heat transfer methods have been successfully applied for the heat flux estimation in capacitively cooled engines where the temperature field is not stationary during the test operation and hence a transient inverse heat conduction method is needed [30–32].

The main concept behind an inverse method for heat conduction problems lies in trying to estimate the boundary conditions (causes) which best fit the measured temperature values (effects) while keeping the physics of the problem intact. In contrast to the capacitive method, no transient calculation is required, since the temperature is in steady-state. Nevertheless, the complexity of the problem increases because a second boundary condition is present in the system, namely the heat transfer between the coolant and the structure. This can be represented by the heat transfer coefficient and the bulk coolant temperature, which are unknown.

Three methods are the most promising for quantifying this additional unknown boundary condition. First, a simultaneous optimization of the heat flux and the heat transfer coefficient at each wall position is possible. This implies that the set of parameters, which are the outputs of the optimization problem, is increased by a factor two (one value for the hot gas wall heat flux and one for the coolant heat transfer coefficient). At the same time, at least two thermocouple measurements are required at the same axial and azimuthal position (for example at different radial positions) to ensure that the number of available information values (thermocouples) is larger than or equal the number of optimization parameters. This method is quite accurate since no modeling of the heat transfer coefficient is required and has been successfully applied for the evaluation of methane/oxygen sub-scale tests [26,33]. The second method would be to utilize a CFD simulation for the coolant side. This significantly increases the computational resources required for the inverse calculation since the flow simulation has to be carried out in each iteration of the optimization loop. Despite the larger computational effort, there is still uncertainty connected to the resulting heat transfer coefficient from the CFD simulation due to the limits of the available turbulence models. Finally, the modeling of the heat transfer can be performed using one-dimensional Nusselt correlations. Despite their empirical nature and lower sophistication level compared to CFD, their fast implementation and minimal computational resources render them attractive for test data evaluation.

In the present work, due to the limited number of thermocouples installed on the examined hardware and the need for short evaluation times, the method utilizing Nusselt correlations is implemented. Similarly to the majority of inverse algorithms, the method is based on an iterative approach as outlined in Fig. 3. The goal of the optimization is to minimize the difference between the measured and calculated temperatures at the measurement locations. The inverse method is implemented in the RoqFITT code which has already been validated for the evaluation of sub-scale rocket engines in Perakis et al. [30].

The starting point of the code is to initialize the temperature in the computational domain and to choose an initial guess for the heat flux. With the initial conditions (temperature field) and the boundary conditions (guessed heat flux) the material properties of the coolant are calculated and the heat transfer coefficient is obtained via the Nusselt correlation. After that, the first step is solving the direct heat transfer problem.

3.1. Direct solver

For the solution of the direct problem, a direct solver is required, which has to be computationally very efficient. This is a strict requirement due to the large number of direct problem evaluations until convergence of the heat flux is achieved. For the solution of the thermal conduction problem, the commercial tool ANSYS Fluent [34] is used and a file-based interface to the code RoqFITT is programmed. The heat conduction equation (Eq. (1)) is solved using a finite volume method in an unstructured grid consisting of 7.5 million cells.

$$\nabla^2 T = 0 \tag{1}$$

The direct solver is used to solve the heat conduction partial differential equation (PDE) in a simplified geometry. The geometry consists only of the combustion chamber and does not include the fluid domain. The effect of the coolant on the temperature field of the structure is included by specifying the modeled boundary conditions.

Only the first segment of the combustion chamber is included in the computational domain. Since the number of the installed thermocouples in the other segments is too low for a sufficient resolution of the heat flux profiles using the inverse method, only the

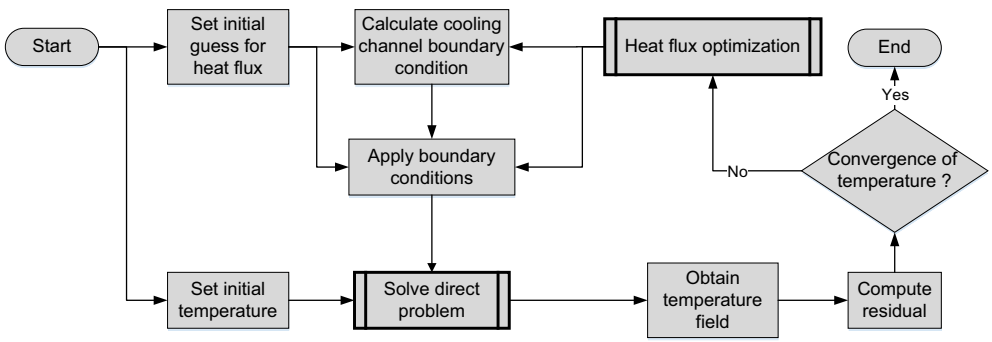

Fig. 3. Inverse heat transfer iterative algorithm.

first part is modeled. The interfaces between the first and second segment as well as between the injector head and the first segment are defined as adiabatic. For the boundary condition at the interface between the first and final combustion chamber segments, an extensive sensitivity analysis has been performed. Specifically, the adiabatic boundary condition was compared to a spatially dependent heat flux, obtained by coupled simulations of the chamber as shown in Rahn et al. [35]. The analysis resulted to the conclusion that the choice of this boundary condition has very small influence on the final heat flux profile. Specifically, between the solutions with the adiabatic and the variable boundary condition, a deviation of ~1% was observed in the heat flux value at the location of the last downstream thermocouple. All other positions upstream appeared to be unaffected by the choice of boundary condition, proving the low sensitivity of the final result on the treatment of this interface. For that reason and to ensure that the rebuilding of the thermal field is purely done on the basis of the measurements without relying on other inputs such as coupled CFD simulations, an adiabatic boundary condition is imposed.

Finally, a natural convection boundary condition is applied to the outer wall with a convective heat transfer coefficient $h = 10\,\mathrm{W/(m^2 \cdot K)}$ and an ambient temperature corresponding to the one measured at each test. An overview of the computational domain and the corresponding boundaries is given in Fig. 4. The shape of the cooling channels is also easy to identify: they begin going almost radially inward towards the hot gas wall and then continue axially parallel to the main flow before bending again radially outwards towards the outlet.

The orientation of the chosen segment with regards to the injector elements is given in Fig. 5. The light gray area shows the entire chamber domain, whereas the area highlighted in dark grey is the modeled domain. The red lines represent the boundaries of the domain. The $\theta = 0^\circ$ and $\theta = 60^\circ$ positions correspond to azimuthal locations directly above an injector element, whereas $\theta = 30^\circ$ and $\theta = 90^\circ$ are symmetry planes between two adjacent elements. Note that the outer radius in Fig. 5 has been reduced from 80 mm down to 40 mm for visualization purposes.

The optimized (hot gas wall) and the modeled (cooling channel) boundary conditions are applied respectively as

$$\dot{q} = \lambda \frac{\partial T}{\partial \mathbf{n}}\bigg|_S \tag{2}$$

$$h_{cc}(T_{cc} - T_w) = \lambda \frac{\partial T}{\partial \mathbf{n}}\bigg|_S \tag{3}$$

In this context **n** is the outward pointing normal vector. Upon solving the direct problem, the temperature field is known and hence the calculated value of the temperature at all the thermocouple positions can be extracted and compared with the measured ones. This residual temperature difference is given as an input to the optimization algorithm.

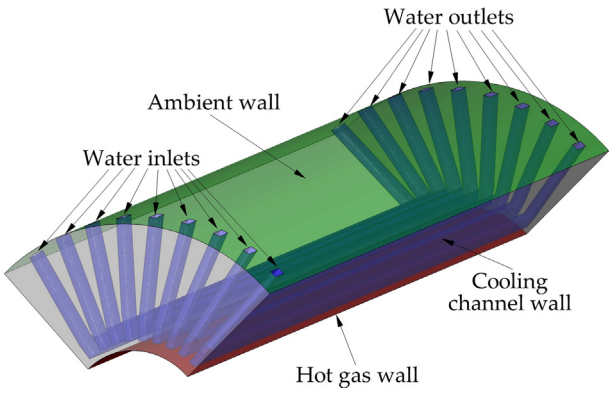

Fig. 4. Schematic view of the first chamber segment.

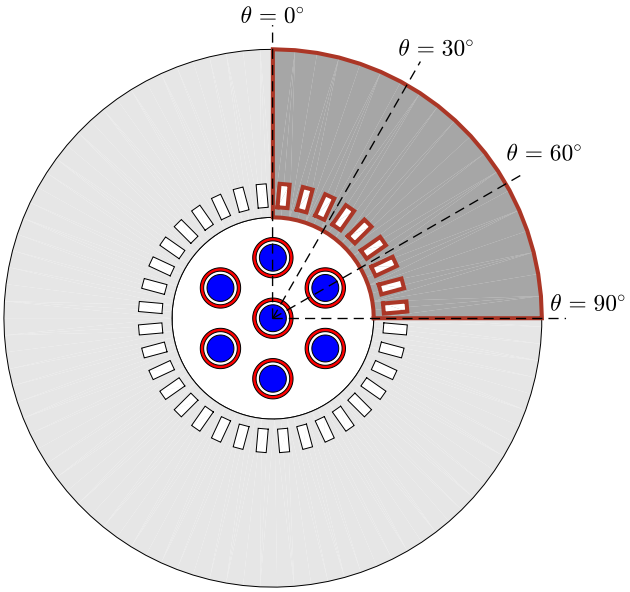

Fig. 5. Cut through the combustion chamber.

3.2. Optimization method

The purpose of the optimization is to minimize the difference between the calculated ($\mathbf{T}_c$) and measured ($\mathbf{T}_m$) temperatures. This residual J which is subject to minimization is defined as in Eq. (4):

$$J(\mathbf{P}) = [\mathbf{T}_m - \mathbf{T}_c(\mathbf{P})]^T [\mathbf{T}_m - \mathbf{T}_c(\mathbf{P})] \tag{4}$$

The vector **P** describes the heat flux values at the parameter points which are subject to optimization. The heat flux is a continuous variable being applied to all the points, however optimizing the heat flux value at every single point in contact with the hot gas would be computationally expensive and render the problem more ill-posed [36]. Having a larger number of optimization points increases the degrees of freedom of the problem without increasing the information input (no additional thermocouple measurements). For that reason, for the method presented here, a parameter is placed only at locations which possess at least one temperature sensor, so the number of parameters N is always smaller or equal to the thermocouple number M. At each time step, the values of the N parameter points are changed to reduce the residual J.

RoqFITT utilizes an iterative update by means of the Jacobi matrix **S**, which serves as a sensitivity matrix describing the change of the temperature at a thermocouple position due to a small change at a specific heat flux parameter value. Its structure is presented in Eq. (5). It was shown in a sensitivity study that the linearity of the Fourier heat conduction equation allows for a calculation of the Jacobi matrix outside of the optimization loop. For that reason the computation of the matrix occurs as a preprocessing step before the calculation and it is saved for future calculations as well. As long as the number and locations of the thermocouples and parameters do not change, the matrix remains unaltered.

$$\mathbf{S} = \begin{bmatrix} \frac{\partial T_1}{\partial P_1} & \cdots & \frac{\partial T_M}{\partial P_1} \\ \vdots & \ddots & \vdots \\ \frac{\partial T_1}{\partial P_N} & \cdots & \frac{\partial T_M}{\partial P_N} \end{bmatrix} \tag{5}$$

The implemented optimization method is based on a linearization of the problem and follows the Newton-Raphson formulation for the solution of non-linear systems [37]. The heat flux at each iteration step k is obtained by solving the algebraic equation

$$\mathbf{S} \cdot \mathbf{P}^{k+1} = \left[\mathbf{T}_m - \mathbf{T}_c(\mathbf{P}^k)\right] + \mathbf{S} \cdot \mathbf{P}^k \tag{6}$$

The process is repeated until convergence is achieved, i.e. until the residual drops beneath a predefined value ε. When this is the case, the calculation is finished and the post-processing and visualization of the results starts. For the present study the convergence condition is that each individual sensor measurement drops beneath the inherent uncertainty of the thermocouple measurements ΔT. Hence ε is set to the accuracy of the used temperature measurement system.

The fact that a Jacobian is obtained outside of the optimization loop increases the computational efficiency of the algorithm dramatically. Convergence occurs in less than 15 iterations with a total computational cost of approximately 4 CPUh on four Intel Core i7-6700 at 3.40 GHz. The calculation of the Jacobian (which has to be performed only once for a given geometry and thermocouple configuration) required less than 10 CPUh on the same workstation.

3.3. Applying the heat flux on the boundary

At each axial position with available temperature measurements, four thermocouples are installed, each one at 0°, 30°, 60° or 90°. In total 8 axial positions are equipped with thermocouples leading to 32 sensors used in each calculation. The possible locations of the thermocouples are shown in the right sub-figure of Fig. 6, where the orange markers represent the 1.5 mm and the red ones the 0.5 mm distance from the hot gas wall.

As mentioned in the description of the optimization algorithm, the heat flux is updated only at specific locations and specifically only at the thermocouples positions projected on the hot gas wall, as indicated in Fig. 6. Special care has to be taken to transform the heat flux from the few locations in the chamber to a continuous variable over the whole boundary domain. A cubic interpolation is used to transform the discrete values to a continuous profile in axial and azimuthal direction. At the symmetry planes (0° and 90°) a symmetry condition is applied for the interpolation of the heat flux in azimuthal direction, meaning $\partial \dot{q}/\partial \theta = 0$. For the axial positions between the last thermocouple and the end of the chamber segment, a linear extrapolation is applied.

3.4. Modeling the cooling channels

For the unknown heat transfer coefficient in the cooling channels, Nusselt correlations for generic pipe flows are implemented. Using the work of Kirchberger et al. [38,39] where correlations where used for the description of the cooling channel heat transfer, the most prominent correlations are examined. Although both the models by Gnielinski [40] and Kraussold [41] showed similar profiles, only the Kraussold model will be discussed. The Kraussold correlation which reads

$$Nu_{cc} = \frac{h_{cc} \cdot d_h}{\lambda} = 0.024 \cdot Re^{0.8} \cdot Pr^{0.37} \tag{7}$$

is a function of the geometry (hydraulic diameter d_h) and material properties as it depends on the heat capacity c_p, thermal conductivity λ, dynamic viscosity μ as well as on the mass flow rate $\dot{m}_{cc}$ (which is needed for the Reynolds number). The temperature dependent properties are obtained using the NIST database [42]. The correction factors for the start-up of the flow [39] was also investigated.

At this point it is important to note that due to the complex geometry of the cooling channels (transition from radially inwards flow to axial flow, rectangular shape), the use of any Nusselt-based correlations will only approximate the real heat transfer coefficient. Studies are planned in order to obtain a more detailed correlation for the coolant heat transfer by running parametric CFD simulations of the geometry and obtaining a correlation using machine learning as in the works of Chang et al. [43] and Scalabrin et al. [44]. For the present analysis a classical correlation by Kraussold, shown to produce reasonable results for rocket engine cooling channels [39] will be shown but the inverse method presented here is not restricted to the use of this particular approximation.

In order to use Eq. (3) for the estimation of the boundary condition and to calculate the aforementioned fluid properties, the average bulk coolant temperature is required. The heating of the coolant (in this case water) is carried out by assuming that the system is in steady state and hence the whole heat is effectively flowing into the coolant. Therefore the coolant temperature at axial position x is given by

$$T_{cc}(x) = T_{cc,in} + \int_0^x \frac{2\pi r_c}{N_{cc}} \frac{\dot{q}}{\dot{m}_{cc} c_p} \mathrm{dx} \tag{8}$$

with heat flux $\dot{q}$ as the average heat flux at the considered differential wall surface.

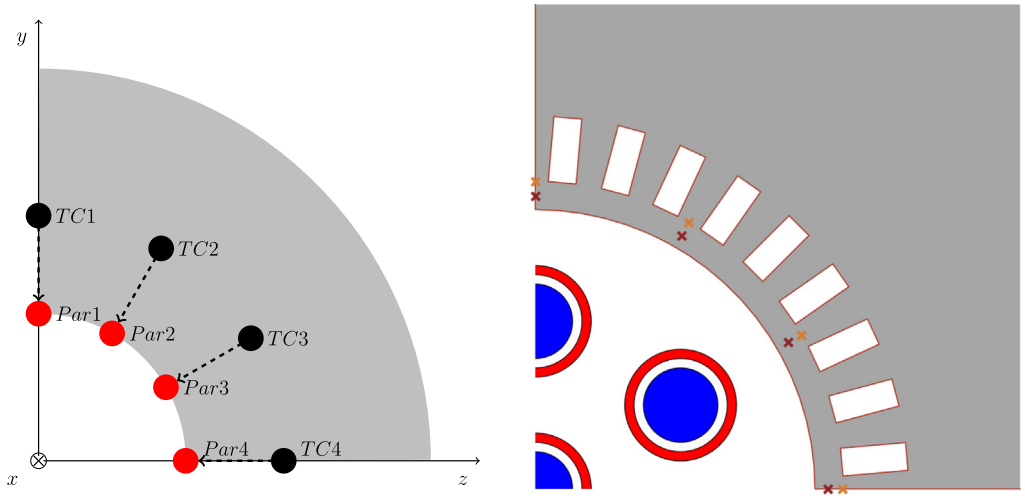

Fig. 6. Definition of parameter points (left) and the locations of installed thermocouples (right).

The computational domain possesses nine cooling channels. Fig. 7 illustrates the contour of the cooling channels projected onto the hot gas surface. The division of the surface above the axial cooling channel parts into nine equally sized strips is visualized, too. The integral heat flow over one of these strips is the energy that heats up the coolant in the corresponding cooling channel. To obtain the coolant bulk temperature distribution in x-direction, the cooling channels are discretized (cf. cooling channel at 5° azimuthal position in Fig. 7). Then the bulk temperature increment is calculated for each cell of the length dx_{cc} by evaluating Eq. (8). For that the integral heat flow within the blue rectangle in Fig. 7 is calculated.

4. Error analysis

For a proper evaluation of the experimental data and a potential comparison with CFD simulations, knowledge of the different error sources as well as the magnitude of the individual errors is necessary. The error sources are usually due to statistical and systematical error of the measured data as well as due to the uncertainties used in the models.

In the case of the RoqFITT code the measurements are restricted to the thermocouple readings. As far as the model is concerned, RoqFITT uses the heat conduction equation with modeled boundary conditions, which introduces additional uncertainty to the system. The potential error sources also comprise the material properties and the treatment of the boundary conditions at the interface with the second segment. Due to the steady-state nature of the problem, thermocouple response delay is not included in the analysis.

Summarized, the uncertainties which have to be included in the error propagation are the following:

- Thermocouple accuracy.
- Thermocouple precision.
- Thermocouple positioning.
- Material properties.
- Boundary conditions.

The individual error sources are documented in detail in Perakis et al. [30] and in this chapter only the specific issues applicable to the multi-element chamber will be discussed.

4.1. Thermocouple accuracy

For the accuracy of the thermocouples, the manufacturer's instrument accuracy ΔT_{acc} is used, which is set to 1.0 K for type T thermocouples. Using the concept of linearization, the heat flux error $\Delta \mathbf{P}_{acc}$ can be obtained by means of the Jacobi matrix, by solving the algebraic system in Eq. (9).

$$\Delta \mathbf{P}_{acc} = \mathbf{S}^{-1} \cdot \Delta \mathbf{T}_{acc} \tag{9}$$

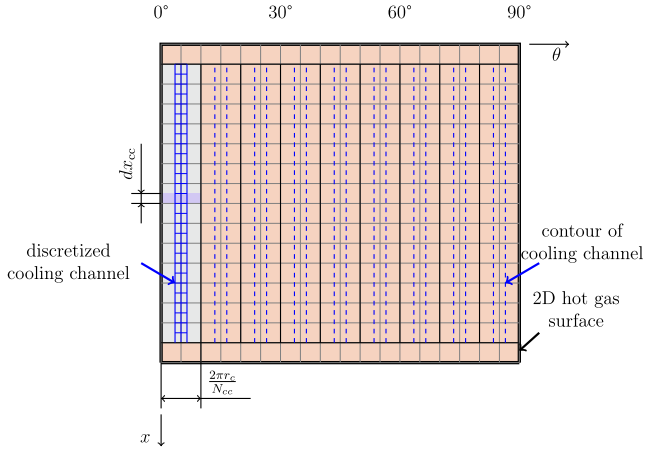

Fig. 7. Discretization of the cooling channels for the water heat-up calculation.

4.2. Thermocouple precision

In case of the steady-state temperature measurements, the precision error is defined as the random fluctuation of the thermocouples readings within a specific time window. The raw thermocouple data is prone to high frequency noise and for that reason the standard deviation of the transient profiles within a time window of 1 s is used. The corresponding heat flux error is given similar to Eq. (9).

4.3. Thermocouple positioning

A further source of uncertainty when using thermocouples is the fact that their exact location is not always known. Due to manufacturing tolerances of the drilling hole in which the sensor is installed, the exact contact point between the copper material of the chamber and the thermocouple tip cannot be predicted with 100% accuracy. In order to take this into account, a post-processing step is introduced in RoqFITT, during which a systematic radial deviation Δr is defined for all thermocouples. The initial radial position of the thermocouples r_0 is hence replaced by $r_0 + \Delta r$. Using the converged solution for the heat flux and the temperature field in the domain, the temperature at the new thermocouple positions can be found and it is used for the estimation of the temperature error:

$$\Delta \mathbf{T}_{loc} = \mathbf{T}_c(r_0) - \mathbf{T}_c(r_0 + \Delta r) \tag{10}$$

A maximal deviation equal to 0.1 mm is used for this hardware. Extensive measurements of the depth of the drilling hole were carried out before the installation of the sensors, and this is the reason for the relatively small devation used in this study. The estimation of the resulting heat flux error is carried out with the Jacobi matrix similar to Eq. (9). This calculation of the positioning error was also carried out by repeating the inverse calculation with modified positions for the thermocouples and the result was compared to the approximation in Eq. (10). Both methods deliver almost identical results for the small location errors assumed here.

4.4. Material properties

For the solution of the steady state heat equation only the thermal conductivity of the material is required and this value is bound to some uncertainty. A deviation from the nominal value λ_0 with the magnitude $\Delta\lambda$ = 10% is assumed.

Due to the steady-state nature of the problem, the inverse calculation is not computationally expensive and hence the repetition of the solution with the modified material properties is not prohibitive. For that reason, the inverse solution is repeated and the resulting heat flux error is simply given by Eq. (11).

$$\Delta \mathbf{P}_{mat} = \mathbf{P}(\lambda_0) - \mathbf{P}(\lambda_0 + \Delta\lambda) \tag{11}$$

4.5. Boundary conditions

In the computational domain of the rocket combustors, the boundary conditions at the surfaces in contact with the second segment and the outer surface have to be modeled. The natural convection was found to have a negligible effect on the final result of the hot gas heat flux and is hence not included in the error prop-

agation analysis. For the second segment interface the adiabatic condition has been compared to a spatially heat flux obtained by Rahn et al. [35]. Upon comparison of the values obtained with adiabatic and variable boundaries, no significant difference was observed and therefore the adiabatic condition is maintained. This is physically justified by the fact that both segments are run in co-flow with the hot gas and hence the axial heat transfer is minimal.

On the other hand, the effect of the coolant heat transfer coefficient and coolant temperature on the uncertainty of the final heat flux is not negligible. In order to quantify this error, using a linear approach as in Eq. (11) is not straightforward, since the bulk coolant temperature is also dependent on the converged heat flux. For that reason the inverse calculation is repeated after convergence with the modified $h_{cc} = 1.15 \cdot h_{cc,Kraussold}$. Here an uncertainty of 15% is assumed for the heat transfer coefficient. Determining this value is difficult since it strongly depends on the geometry and requires detailed CFD simulations for each load point. The quantification of the error introduced when using a Nusselt correlation for the description of wall heat transfer in rocket cooling channels has been examined by Haemisch et al. [33] for methane and hydrogen but there are limited works dealing with water as coolant. The uncertainty of 15% is chosen only to provide a reference for the propagated wall heat flux error. Studies which are beyond the scope of the present work have been planned in order to quantify the actual deviation of the chosen correlation and to provide an improved correlation by the use of parametric studies and deep learning algorithms [43].

The resulting heat flux uncertainty is given by

$$\Delta\mathbf{P}_{corr} = \mathbf{P}(h_{cc}) - \mathbf{P}(h_{cc,Kraussold}) \tag{12}$$

For the water temperature at inlet, a similar method is implemented, with a temperature deviation $\Delta T_w = 1$ K.

$$\Delta\mathbf{P}_{Tw} = \mathbf{P}(T_w + \Delta T_w) - \mathbf{P}(T_w) \tag{13}$$

Summing up all the error sources according to Eq. (14) results in a total uncertainty $\Delta\mathbf{P}_{tot}$ between 10% and 30% of the converged heat flux value at each parameter location.

$$\Delta\mathbf{P}_{tot} = \sqrt{\Delta\mathbf{P}^2_{acc} + \Delta\mathbf{P}^2_{prec} + \Delta\mathbf{P}^2_{loc} + \Delta\mathbf{P}^2_{mat} + \Delta\mathbf{P}^2_{corr} + \Delta\mathbf{P}^2_{Tw}} \tag{14}$$

The relative magnitude of the uncertainty compared to the calculated value for each of the axial positions is given in the left subfigure of Fig. 8. The relative total error is largest for the first axial position. This is expected due to the small temperature increase and heat flux value at this location, which makes the temperature measurement errors (both in material and in the water) more significant. For all remaining axial positions, relative values between 10% and 15% are obtained.

The main contribution (around 90%) results from the used cooling channel correlation, whereas the accuracy, precision and water temperature errors are negligible with the exception of the first axial position. A detailed analysis of each contribution is shown in the right sub-figure of Fig. 8. It is observed that the magnitude of the error induced by the material properties alternates between two consecutive axial positions. This is due to the different radial distances of the thermocouples in each plane. Planes with thermocouples closer to the hot gas wall are less tolerant to the variation of the heat flux conductivity, since the thermal gradients are higher at their position. In the same note, they are also more affected by the positioning error, whereas they appear to be more resistant to the correlation, because of the larger distance from the cooling channels.

5. Results

In this chapter we present the heat flux results obtained with the inverse method implemented in RoqFITT for different operating conditions.

In the context of the national research program Transregio SFB-TRR 40 on “Technological Foundation for the design of thermally and mechanically high loaded components of Future Space Transportation System”, a test case using the multi-element chamber was defined during the Summer Program 2017 with the purpose of motivating groups to simulate the flow conditions in the combustion chamber and accurately predict the pressure and heat flux profiles at the wall. The available experimental data included pressure measurements and average calorimetric heat flux values for each segment due to the absence of a reliable inverse method. The test case comprises an operational point at 20 bar and O/F = 2.6, with the fuel and oxidizer being injected at ambient temperature in gaseous form.

A large number of groups carried out independent calculations of the turbulent combustion in the rocket engine and the results were compared to each other and to the available measurements [28,35,45,25]. Deviations between the solutions of the individual groups regarding the azimuthal distribution of the wall heat flux increased the motivation for an inverse method with high spatial resolution.

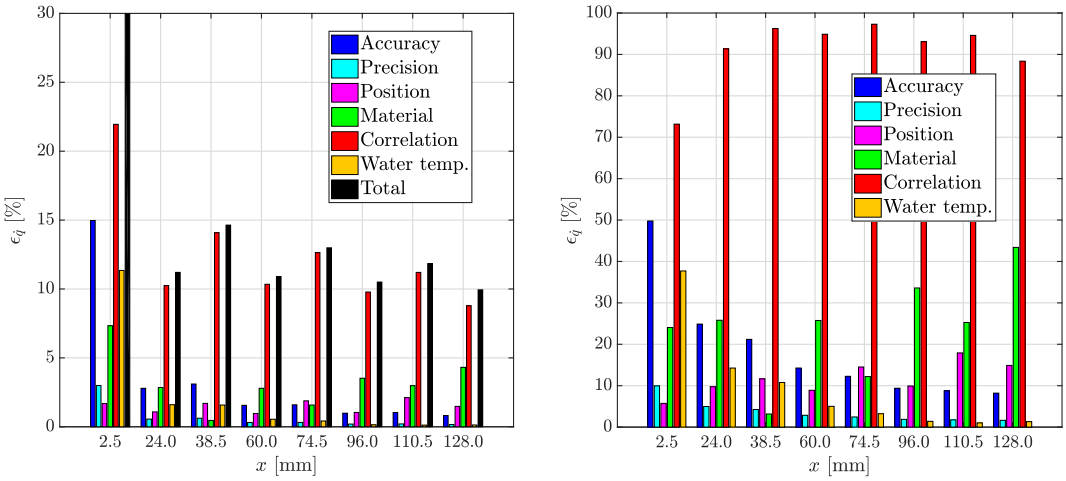

Fig. 8. Relative error (left) and individual error contributions (right) at different axial positions.

5.1. Temperature profiles

The only information available used by the inverse method for the reconstruction of the thermal field are the temperature sensor measurements. Those are shown in Fig. 9, where the circles represent the measurements at 1.5 mm from the hot gas wall and the diamonds the ones at 0.7 mm. In the same graph the reconstructed temperature field stemming from the inverse method is also shown. 0° and 60° correspond to the two neighboring injector elements.

As far as the measurements are concerned, a general increase of the temperature with increasing axial position is observed. Since the mixing and energy release is still ongoing in the first segment, an increasing heat load and hence temperature reading is expected as the flow moves downstream of the injector. Moreover, a slight asymmetry in the readings is observed. It would be expected that positions 0° and 60° have almost identical results, as should 30° and 90°. Since this deviation appears to be systematic, i.e. the values at 0° appear to be larger than the ones at 60° for all axial positions, a faulty thermocouple installation is excluded since that would be an error of statistical nature. Instead a slight asymmetry of the co-axial injectors (either due to the manufacturing or the assembly) is assumed to be the cause.

The reconstructed field shown in Fig. 9 matches the measured values within the defined tolerance of the inverse method. The profiles at 0.7 mm (solid lines) have higher values since they are closer to the hot gas wall, whereas the 1.5 mm show a much more prominent cooling channel footprint, as they are closer to the cooling channels. Specifically, the wavy pattern results from the geometry of the cooling channels, with the temperature minimums corresponding to positions between two channels, and the maximums to positions directly under the channels.

5.2. Azimuthal heat flux profiles

The corresponding heat flux profiles are illustrated in Fig. 10. For each axial position, the heat flux resulting from the inverse method is plotted with the markers representing the values at the parameter points and the solid lines representing the azimuthal heat flux profile applied at the wall. The uncertainty intervals calculated as described in Section 4 are shown as shadows and amount to ±10–30% of the average values.

It is easy to notice by looking at Fig. 10 that an injector footprint is visible in the heat flux data. Specifically, for the first 60 mm of the chamber a local maximum directly above the injector is observed with a local minimum at the positions between two elements (30° and 90°). Despite the asymmetry produced by the temperature readings, all four available axial positions show a similar trend.

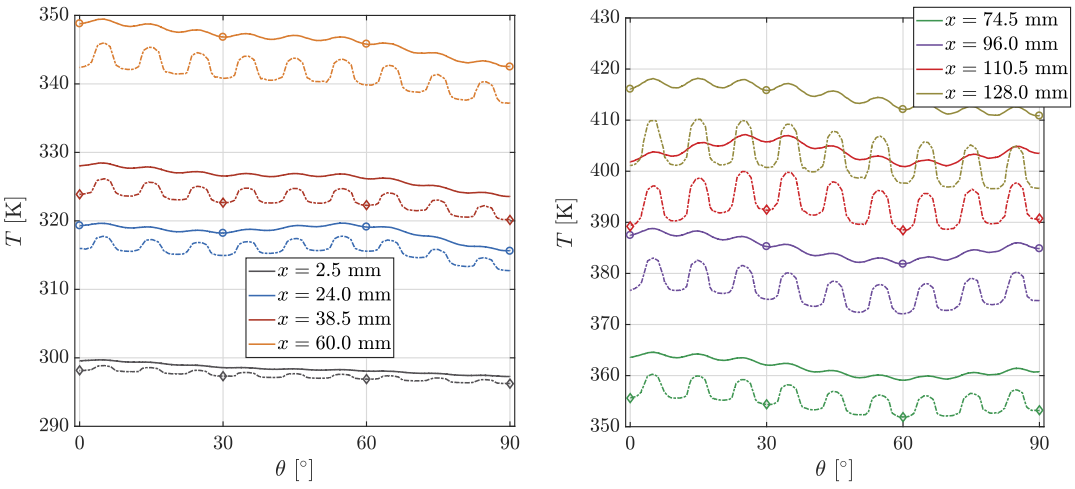

Fig. 9. Measured and calculated temperature at 0.7 and 1.5 mm from the hot gas wall. Solid lines correspond to 0.7 mm and the dashed ones to 1.5 mm.

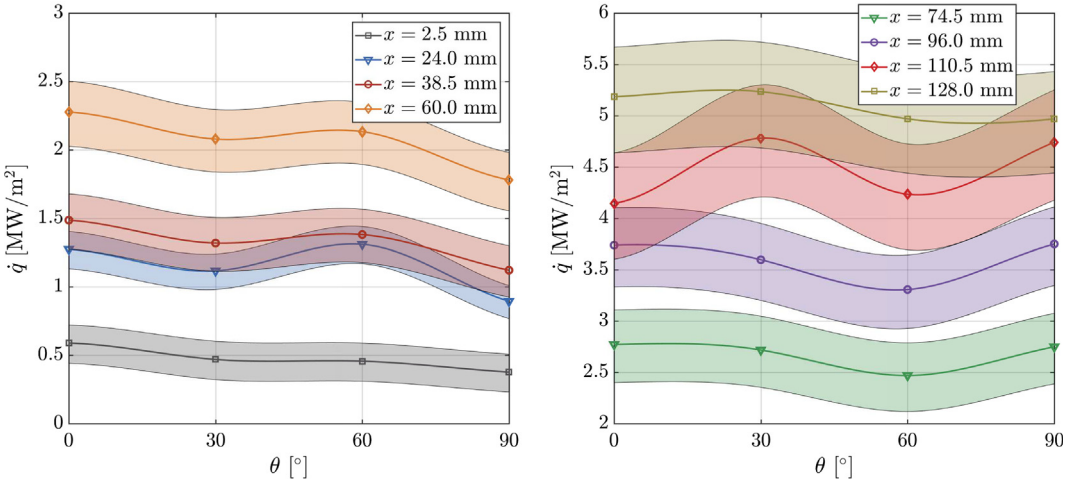

Fig. 10. Heat flux profiles along the azimuthal direction for different axial positions. The corresponding uncertainty intervals are also shown.

Moving towards positions downstream, a shift is observed in the measured heat flux profiles. Starting at around 74.5 mm the heat flux at the 60° position appears to drop below the values at 30° and 90°, indicating a change in the injector/injector and injector/wall interaction. Due to the asymmetry in the measured temperatures, the 0° heat flux undergoes this shift at a later downstream position and the profile becomes symmetric again at the 110.5 mm position. After this axial location, the injector footprint is inverted compared to the initial positions close to the face-plate.

For axial positions close to the face-plate, the flames from the individual injector elements are almost cylindrical and interact minimally with each other. Therefore, the heat transfer coefficient directly above the injector is maximal due to the distance between element and wall being smallest. As the heat release in the coaxial shear layer of each element increases and leads to a radial expansion of the jet outwards, the interaction between the jets is amplified. In an effort to expand radially against each other, the flames build a stagnation flow between two neighboring elements. Due to the central element jet also expanding radially outwards, the stagnation flow is forced towards the wall and increases the local heat transfer at the locations between the injectors. Further downstream (for positions which are unfortunately in the other 3 segments of the TUM chamber and hence not shown in the inverse method results) the mixing is further increased and a homogeneous flow is achieved, leading to a smoother heat flux distribution where the injector footprint is no longer visible. This pattern is also observed in CFD simulations in Section 5.4.

It is important to note that the injector footprint observed in Fig. 10 is not directly visible in the thermocouple readings shown in Fig. 9. Although some of the effects can be identified (different behavior in the first and second part of the segment), due to the asymmetry of the measurements, the injector footprint is obscured. Only after the evaluation of the test data with the inverse method is the footprint visible in terms of heat load profiles. This is an additional motivation for the use of the inverse method for the evaluation of the test results, as the raw thermocouple data cannot convey all the physical information, since they are the result of multiple physical effects which have to be separated.

The circumferential variations in heat flux appear to be in agreement with the physical arguments resulting from the consideration of the flame/flame interaction within the chamber. Nevertheless, it has to be noted that the observed variations are of the same order as the error bands in Fig. 10. When trying to assess the reliability of the obtained profiles it is essential to include the nature of the uncertainties in the discussion. Specifically, as demonstrated in Section 4, the correlation for the cooling water heat transfer coefficient contributed by approximately 90% to the total uncertainty. This error source is however systematic and acts more as a bias to the obtained results. Since all cooling channels have identical geometry and mass flow rates, it is expected that their flow-field is very similar for the same axial position. For that reason they should also exhibit similar heat transfer coefficients, which is confirmed in the left sub-figure of Fig. 13. There, the relative deviations in each axial plane do not exceed 1%. From this argument follows that even if the modeled heat transfer coefficient has a large deviation from the experimental one, the error should act as a bias for all azimuthal positions, thereby leading to a shift of the entire heat flux profile, while preserving the circumferential variations.

The effect of the injector footprint that the inverse method tries to capture requires a resolution of at least 30°, namely equal to half the angular distance between the injectors. The chosen hardware is equipped with sensors satisfying this minimal angular resolution, meaning that any heat flux information with a shorter angular wavelength will not be captured by the method. An increase in the number of installed sensors or a rotation of the hardware after every test repetition as in the work of Suslov et al. [26] would be required for a more detailed profile.

Finally, the effect of the domain size was also investigated in order to quantify the influence of the temperature asymmetry which was reported in Section 5.1. For this study the 90° domain presented in the results so far was compared to simulations using a smaller, 60° domain. For the smaller domain, two separate studies were performed: one using the measurements at 0°, 30° and 60° and with the 30°, 60° and 90° values. The results in Fig. 11 illustrate that all three measurement sets lead to similar results. Both the magnitude and the form of the profile are in good agreement for the different domain choices. The only measurable difference occurs at the 30° location. At this point the asymmetry of the measurements is more prominent and the assumption of $\partial\dot{q}/\partial\theta$ at the symmetry plane is violated. This results in a maximal error of 5% compared to the full 90° domain. Hence, this study shows that a smaller domain could also be used, consisting of only 60°. The benefits of reducing the domain size however are not so dominant, as the computational speed of the method is already very low as reported in Section 3.

5.3. Comparison with calorimetric method

The axial evolution of the heat flux values for the four azimuthal positions which are equipped with thermocouples is shown in the left sub-figure of Fig. 12. The uncertainty intervals are omitted for visualisation purposes. One observes that although the 0° and 60° profiles start higher than the 30° and 90° ones, at approximately 70 mm from the face-plate, the 90° heat flux surpasses the 60° value, and after 100 mm the same occurs between 0° and 30°. The heat flux keeps increasing for all axial positions, indicating that the combustion is not complete yet, which is expected as the length of the first segment does not exceed 150 mm.

Looking at the azimuthally averaged profile and globally average heat flux value in the right sub-figure of Fig. 12, a comparison with the calorimetrically determined value can be made. Using the difference of incoming and outcoming water enthalpy flow, the calorimetric heat flux lies at 3.40 MW/m^2 with a relative error of approximately 10%. The error comes from the uncertainty of the water mass flow measurement (around 1% of the nominal value) and a 1 K accuracy of each water thermocouple. The average value obtained via the inverse method on the other hand is equal to

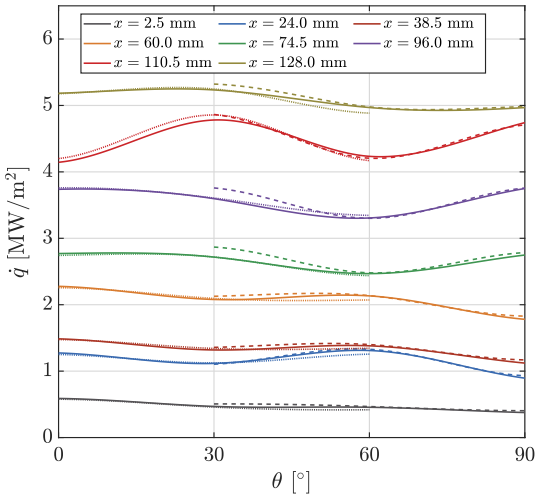

Fig. 11. Azimuthal heat flux results for different sets of measurement. The solid lines represent the 0–30–60–90° configuration, the dotted one the 0–30–60° and the dashed one the 30–60–90°.

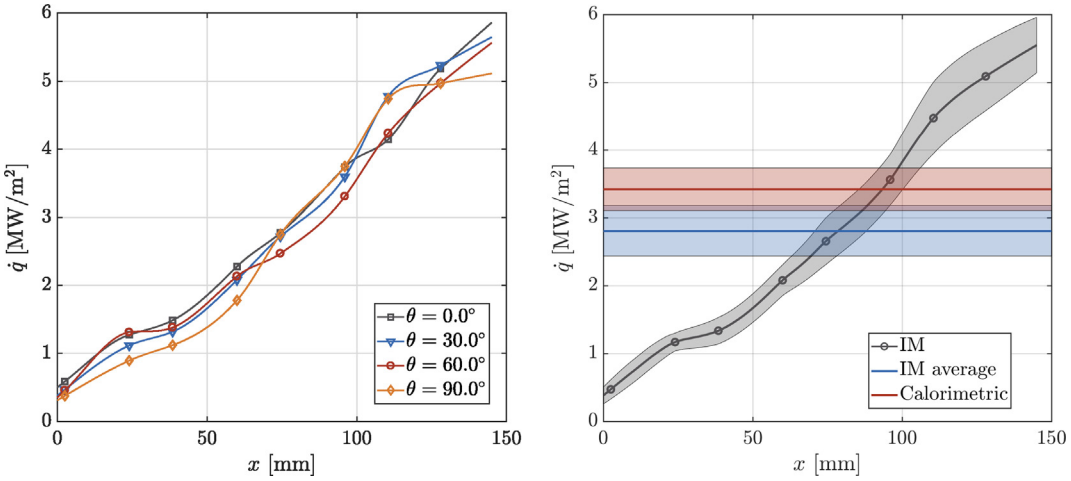

Fig. 12. Heat flux profiles along the axial direction for different angular positions (left) and average heat flux along axial position (right).

2.85 MW/m^2 with a 11.5% uncertainty. Note that this uncertainty strongly depends on the assumed error induced by the Kraussold correlation, which was arbitrarily set to 15%. The uncertainty intervals of the two heat flux evaluation methods intersect, which serves as a validation for the heat flux level predicted by the inverse method.

The deviation between the two methods is attributed to the error introduced by the generic Nusselt correlation for the specific geometry, which could underestimate the heat transfer coefficient within the cooling channels. Due to the shape of the channels, a recirculation zone is namely expected at the interface between the radial part and the flow-parallel part of the channel, which could theoretical increase the local turbulence and heat pickup. The heat flux obtained by the inverse method is directly proportional to the heat flux exiting the domain through the cooling channels. Hence too small a value for h_{cc} would directly cause a lower wall heat flux compared to the experiment. Further studies are planned in order to evaluate the validity of the chosen correlation using comparison with CFD simulations of the cooling channels and to derive a new correlation fitted for the present flow configuration.

The lower heat flux compared to the calorimetric method, also affects the calculated water temperatures. In Fig. 13 the temperature profile for four of the nine cooling channels is shown along with the average calculated and average measured water outlet temperature. The injector footprint has an impact on the water heat-up, as the cooling channels close to the injector elements (5° and 55°) start with a higher temperature than the corresponding ones between the elements (25° and 85°). As soon as the shift in the location of the heat flux maximum occurs, the gradient of the water temperature at 25° and 85° also rises faster, and the values catch up close to the outlet.

The average water outlet temperature of all nine channels originating from the inverse method is 302.5 K, which lies approximately 2.3 K lower then the measured value. The difference can be attributed to the lower heat flux predicted than the inverse method, as the water heat-up is directly proportional to the integral heat load. The difference of 2.3 K corresponds to a relative error of around 11.5%, which is comparable to the deviation of the calorimetric and inverse heat flux evaluations.

5.4. Comparison with CFD

The previously described test case has been the subject of numerical investigation by various groups, which have utilized CFD models to describe the physical phenomena taking place within the combustor with special focus in the injector/injector and injector/wall interaction. A summary of the RANS simulations

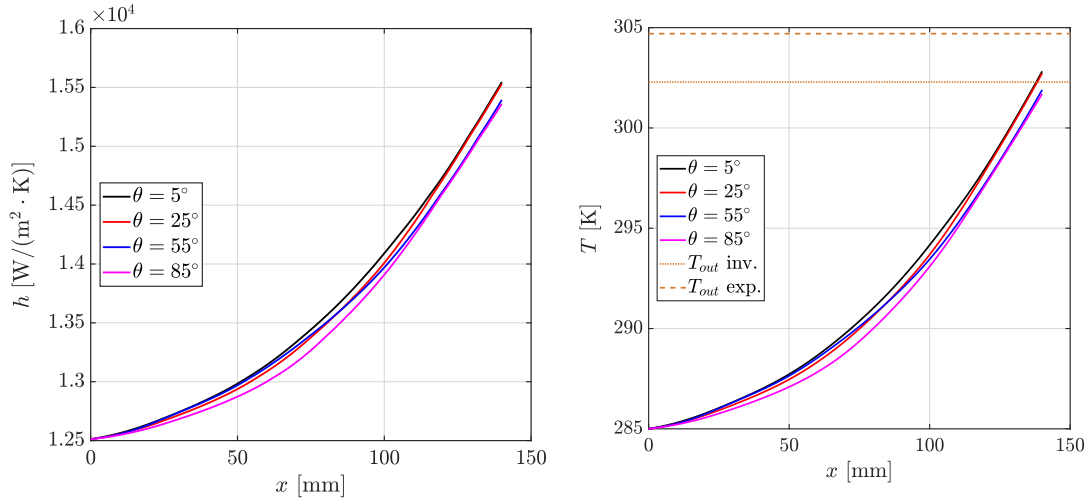

Fig. 13. Heat transfer coefficient (left) and water temperature (right) in the cooling channels.

results can be found in Perakis et al. [28]. Due to the availability of CFD results, it is interesting to compare the results acquired with the inverse method with the ones using RANS models for the simulation of the turbulent combustion. This comparison does not serve as a validation of the inverse method but rather as an effort to examine whether the profiles obtained by RoqFITT can be explained by effects observed in the CFD results and which cannot be measured directly in the experiment as they are linked to flow and energy release properties.

The results presented in this section are generated from a simulation of the hot gas in the thrust chamber using the frozen flamelet model [46] with the skeletal chemical mechanism by Slaviskaya et al. [47] for the chemistry modeling. For the turbulence modeling the standard k-ϵ model proposed by Launder and Spalding [48] is implemented. A 3D domain consisting of 30° (corresponding to the minimal symmetry of the chamber) is utilized and the Reynolds-Averaged Navier-Stokes equations are solved with the ideal gas equation for state. For the wall boundary condition, two methods were compared to each other: one using the experimental thermocouple measurements as Dirichlet boundary conditions and a second one where a conjugate heat transfer was applied by fully-coupling the hot gas, structure and cooling channels. Both methods showed almost identical results for the heat flux in the first segment and hence no distinction is required in the present comparison. More details about the setup can be found in Perakis et al. [45].

First a comparison between the average axial heat flux profile of the two methods is given in Fig. 14. The error-bars are shown only for the axial profile and omitted for the average values (both calorimetric and inverse) to make the figure easier to read. The first observation is that the axial profile of the CFD heat flux is quite similar to the inverse one. Starting from the positions close to the injector, the heat flux appears to rise before dropping shortly at around 10 mm from the face-plate. This indicates the location of a recirculation zone, which creates a stagnation point and hence an increase in the local heat transfer. The inverse profile shows a similar trend, but not so prominent, as a slight plateau is achieved at 25 mm. Due to the axial resolution of the heat flux, it is difficult to resolve the small recirculation zone which is predicted by the CFD, but the small drop in the heat flux increase indicates that this effect is still captured by the temperature measurements.

Downstream of this position both method predict a steady increase of the heat flux value and after 110 mm they both show a slower increment, as the profile starts flattening out. This is caused by the build-up of the thermal boundary layer at the wall and the fact that the heat release in the chamber is reduced for positions further downstream.

When examining the average values, the CFD simulation delivers 2.93 MW/m^2, which is comparable to the inverse method result and lies around 14.5% lower than the calorimetric value for this segment.

The azimuthal profiles are also topics of large interest and therefore selected axial planes are shown in Fig. 15. The CFD results are copied along the azimuthal direction as they are symmetric (RANS simulation). Regarding the absolute value of the heat flux, both the simulation as well as the inverse evaluation of the test data show similar levels, which can also be deduced by looking at Fig. 14. Some discrepancies are however noticed in the qualitative form of the profiles. It is evident that the low resolution caused by the positioning of the thermocouples does not allow for a detailed profile as in the case of the CFD. Specifically, the presence of a complicated pattern for positions between two injector elements (0° and 60°) is visible. Since this large-scale structure is finer than the resolution allowed by the thermocouple installation, this cannot be detected with our method.

Despite the inverse method profiles being coarser, they are still able to capture some of the effects found in the CFD. Starting with the first positions close to the face-plate (left sub-figure), both CFD and inverse method show a higher heat flux above the injectors (0°, 60°) than between them (30°, 90°). An additional local maximum at the ±10° positions left and right of each injector is also a result of the CFD simulation, which is a consequence of a secondary flow pattern as explained in detail in [45,28]. For the positions further downstream (right sub-figure), both methods show a shift in the maximum location. After 110 mm, the CFD heat flux values appear to shift, leading to global minima directly above the injector locations (0° and 60°). The main culprit for this change of the pattern is the increasing interaction of neighboring jets, which leads to hot gas being pushed towards the wall between the elements. It is hence quite assuring that the pattern observed in the inverse results and which was described in detail in Section 5.2, is not an artifact of the thermocouple measurements but rather a physical phenomenon supported by the CFD result.

For a more detailed comparison it is suggested that additional instrumentation shall be installed and a repetition of the tests shall be carried out.

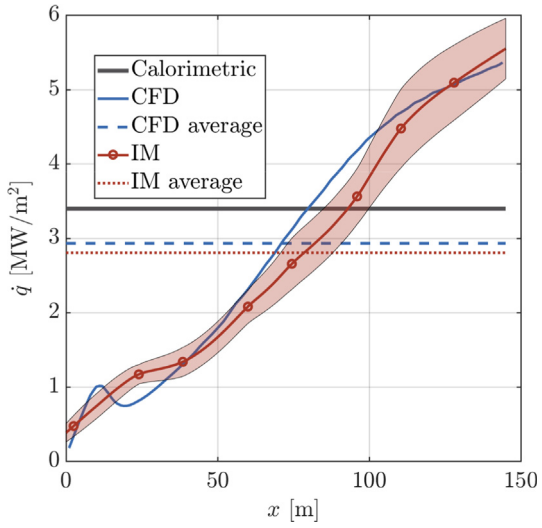

Fig. 14. Axial and average heat flux profile for the CFD simulation and the inverse method. The calorimetric method is also shown for reference.

5.5. Load points comparison

Apart from the 20 bar, O/F = 2.6 test case presented so far, the chamber has also been operated at mixture ratios 3.0 and 3.4 and all three load points have also been repeated for a 30 bar nominal chamber pressure. Due to the gaseous injection of the propellants, the mixture ratio influences the velocity ratio and momentum flux ratio of methane and oxygen and hence the dynamics in the vicinity of the injection system.

These effects are visible in the axial profiles of Fig. 16, where the heat flux of the 20 and 30 bar cases is plotted. Along with the axial profiles, the average values are shown (solid line) as well as the calorimetric measurement (dashed line). The error bars are not included for visualization purposes.

It is observed that all three load points have quite similar average heat flux values in this segment. In fact, the discrepancy between the inverse and the calorimetric method appears to be almost identical for all O/Fs and both pressure levels. It is important to note that the maximal heat flux for the inverse evaluation of the 20 bar case is around 6 MW/m^2, whereas for the 30 bar case it is 8 MW/m^2. The expected rise in the heat load with increasing pressure is also reflected in the calorimetric measurements.

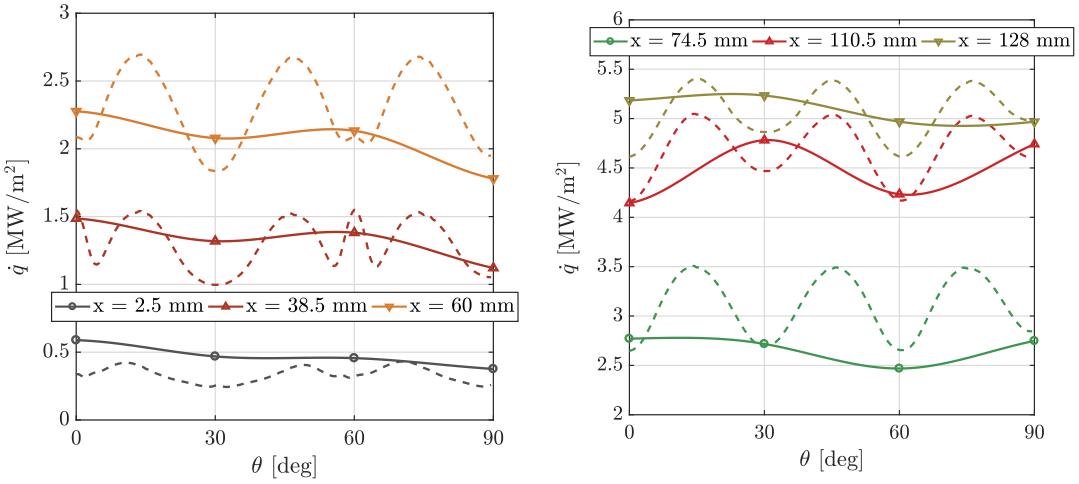

Fig. 15. Heat flux profiles along the azimuthal direction for different axial positions for the inverse method (solid line) and the CFD simulation (dashed line).

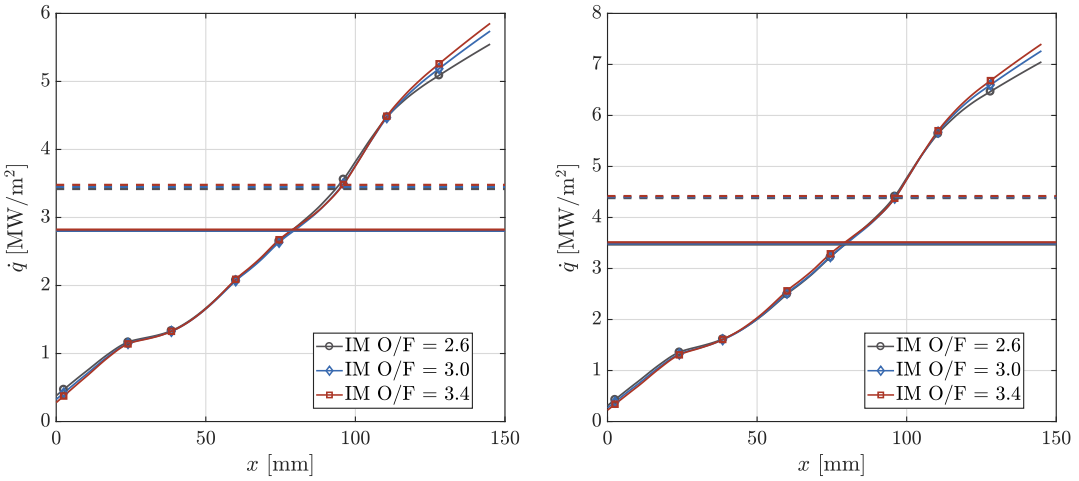

Fig. 16. Heat flux profiles along the axial direction for different O/F values for the 20 bar (left) and 30 bar (right) cases.

A more detailed look into the exact profiles is given in the plots of the azimuthal distributions in Figs. 17 and 18. Starting with the positions close to the injector, the lower O/F (O/F = 2.6, solid line) produces the highest heat flux. Moving downstream, for the first 60 mm the higher O/F test cases (O/F = 3.4, dashed line) appear to lead to a larger thermal stratification compared to the O/F = 2.6, i.e. to a more visible injector footprint. The values at 0° and 60° appear to increase with increasing O/F, whereas the positions between the elements (30°, 90°) show the opposite pattern. The explanation is given by the difference in momentum flux ratio and velocity ratio. If the mixing is shifted downstream in the high O/F cases due to the large inertia of oxygen pulling the methane annulus with it, it is expected that the jets retain their almost cylindrical form and do not mix laterally with the neighboring flames. For lower O/F on the other hand, due to the higher methane velocity, a larger expansion is predicted and therefore a better mixing close to the face-plate inducing a more homogeneous flow and a reduced stratification.

This effect prevails up until the first 74.5 mm. At this point the chemistry becomes more dominant and a break-even point is observed where the hydrodynamic and chemical effects cancel out and the heat flux values appear almost independent of the O/F. For the final downstream location however (128 mm), the mixing has progressed and the chemical effects have definitely overtaken the initial footprint, leading to the higher O/F cases having a larger overall heat flux due to the higher gas temperature).

This phenomenon has been explored in previous studies with rocket combustor demonstrators operated using the same injector elements as the 7-element chamber of this work [49,30]. Due to the higher momentum of the central oxygen jet with higher O/F, the mixing and energy release zone is shifted downstream, and for positions closer to the injector, a lower heat load is achieved. For positions further downstream however, the chemistry dominates and since the combustion temperature of the higher O/F is larger (closer to stoichiometry), the heat flux is also expected to be higher. This explains why the lower O/Fs start with a higher heat flux for $x = 0$ mm and end up with a lower value at the end of the segment.

All the observed effects are within the uncertainty limits which result from the error analysis presented in Section 4. However, the physical motivation behind the interpretation of those phenomena has been shown in previous studies and validated with CFD simulations of similar configurations [49]. Moreover, using the same argumentation as in Section 5.2, the main contribution of the uncertainty is the heat transfer correlation error and it should lead to a homogeneous bias in the heat flux results, hence not affecting the relative profiles and the resulting physical interpretation.

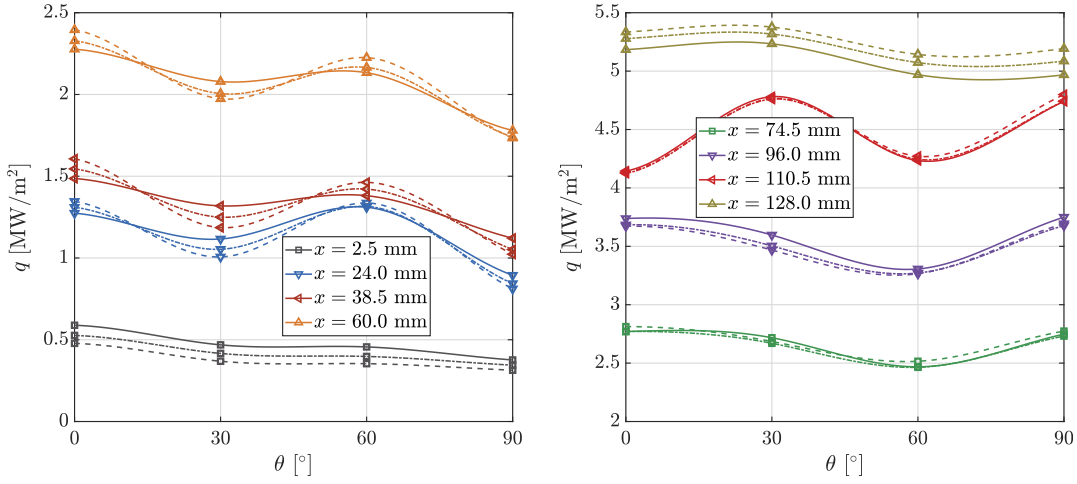

Fig. 17. Heat flux profiles along the axial direction for different axial positions at 20 bar. Solid line: O/F = 2.6, dash-dot line: O/F = 3.0 and dashed line: O/F = 3.4.

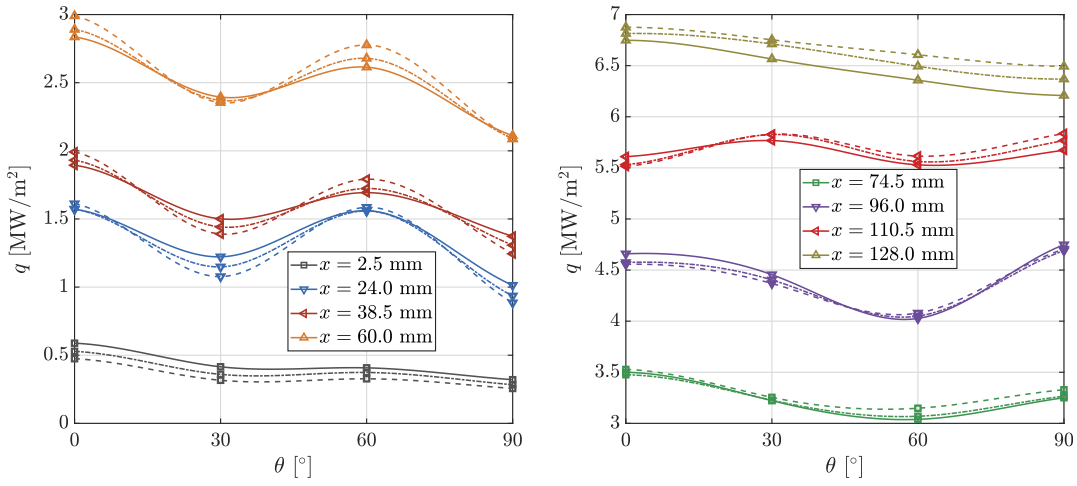

Fig. 18. Heat flux profiles along the azimuthal direction for different axial positions at 30 bar. Solid line: O/F = 2.6, dash-dot line: O/F = 3.0 and dashed line: O/F = 3.4.

6. Conclusion

The evaluation of heat flux profiles in sub-scale engines is crucial for the understanding of the underlying physical and chemical processes defining the injector performance, the injector/injector and injector/wall interaction, mixing and energy release in the chamber. The inverse heat transfer method implemented in RoϱFITT is intended for the analysis of temperature and heat flux distributions in actively cooled rocket thrust chambers.

Similar to previous methods used for the estimation of heat fluxes in capacitive hardware, the inverse method presented in this work relies on an iterative optimization method with the objective of minimizing the temperature difference between the measured and the calculated values. The update of the heat flux parameters at each iteration is carried out using a pre-calculated Jacobi matrix via the Newton-Raphson method. This results to a very efficient optimization algorithm requiring minimal computational resources. The use of thermocouple measurements at different circumferential and axial positions allows for the resolution of axially and azimuthally varying heat loads.

The method can complement calorimetric methods for the evaluation of experimental tests, as it can resolve axially varying loads with much higher spatial accuracy. Compared to gradient methods which require at least two thermocouples per location, the inverse method has demonstrated that one thermocouple per location is sufficient. Compared to the calorimetric method, an axial evolution of the heat flux with much higher resolution is achieved. The two methods agree within 15% with the main reason for this deviation being attributed to the chosen correlation for the heat transfer in the cooling channels. Studies are planned in order to improve the Nusselt correlations by adjusting them to the specific flow conditions examined. Moreover, compared to inverse methods using CFD for the modeling of the coolant flow, a dramatic speed-up is introduced, whereas compared to inverse methods based on simultaneous optimization of wall heat flux and coolant heat transfer coefficient, the number of required installed thermocouples is reduced by a factor of at least 2.

The attractiveness of the new method is its ability to also resolve the azimuthal variation of the heat flux. Using the coarsest possible thermocouple installation in circumferential direction, it was shown that injector footprints can be obtained. This gives information about the interaction of the injector elements without the need for the repetition of the experiments with rotation of the hardware as was proposed by previous methods. Of course, to increase the resolution of the heat transfer in azimuthal direction and to provide a more quantitative comparison with the CFD simulations, a higher number of sensors would be needed. The uncertainty introduced by the Nusselt correlation is expected to

introduce a bias error in the heat flux levels, influencing their absolute level but not their relative variation, hence still allowing the deduction of physical arguments from the obtained azimuthal trends.

When applied for the evaluation of a GCH_4/GOX multi-injector rocket combustor operated at 20 and 30 bar, insights into the physical phenomena in the chamber were obtained. An interesting effect in the circumferential heat flux profile is an observed shift in the location of the local maxima, occurring at around 70 mm distance from the injection plane. This also appeared to be in agreement with CFD simulations of the same load point and can be explained by the secondary flow structures created by the flame/flame interaction. Finally, a comparison between different load points demonstrated that the effect of the velocity and momentum flux ratio on the wall heat loads can be captured by the inverse method. The results confirm that the hydrodynamic effects close to the face-plate dominate leading to higher heat flux for low O/F load points, whereas further downstream the higher O/F produces a larger thermal exchange due to the higher temperature.

It has been shown that the inverse heat transfer method can be applied to rocket engine applications with active cooling for the estimation of the heat loads with minimal computational resources leading to a higher spatial resolution than calorimetric methods. Although only steady state effects were examined in this work, the method could be implemented in a time loop, leading to the capturing of transient effects which may apply during start-up transients and potential combustion instabilities. Finally, the method will be applied for the evaluation of further experimental load points and serve as a validation for new CFD models describing the hot gas flow.

Declaration of Competing Interest

None.

Acknowledgements

The authors would like to thank Ms. Simona Silvestri for providing the experimental data and Mr. Daniel Rahn for providing the heat flux data at the interface with the second chamber segment. Financial support has been provided by the German Research Foundation (Deutsche Forschungsgemeinschaft DFG) in the framework of the Sonderforschungsbereich Transregio 40.

References

[1] J.B. Olansen, Project morpheus: Lander technology development, in: AIAA SPACE 2014 Conference and Exposition, 2014, p. 4314.
[2] J.C. Melcher, R.L. Morehead, Combustion stability characteristics of the project Morpheus liquid oxygen/liquid methane main engine, in: 50th AIAA/ASME/SAE/ASEE Joint Propulsion Conference, 2014, p. 3681.
[3] A. Iannetti, N. Girard, N. Ravier, E. Edeline, D. Tchou-Kien, PROMETHEUS, a low cost LOX/CH4 engine prototype, in: 53rd AIAA/SAE/ASEE Joint Propulsion Conference, 2017, p. 4750.
[4] M. Rudnykh, S. Carapellese, D. Liuzzi, L. Arione, G. Caggiano, P. Bellomi, E. D'Aversa, R. Pellegrini, S. Lobov, A. Gurtovoy, et al., Development of LM10-MIRA LOX/LNG expander cycle demonstrator engine, Acta Astronaut. 126 (2016) 364–374.
[5] E. Musk, Making humans a multi-planetary species, New Space 5 (2) (2017) 46–61.
[6] J.S. Kim, H. Jung, J.H. Kim, State of the art in the development of methane/oxygen liquid-bipropellant rocket engine, J. Korean Soc. Propul. Eng. 17 (6) (2013) 120–130.
[7] T. Kato, D. Terakado, H. Nanri, T. Morito, I. Masuda, H. Asakawa, H. Sakaguchi, Y. Ishikawa, T. Inoue, S. Ishihara, et al., Subscale firing test for regenerative cooling LOX/methane rocket engine, in: 7th European Conference for Aeronautics and Space Sciences (EUCASS), 2017.
[8] H. Asakawa, H. Nanri, K. Aoki, I. Kubota, H. Mori, Y. Ishikawa, K. Kimoto, S. Ishihara, S. Ishizaki, The status of the research and development of LNG rocket engines in japan, in: Chemical Rocket Propulsion, Springer, 2017, pp. 463–487.
[9] O.J. Haidn, Advanced rocket engines, Adv. Propul. Technol. High-Speed Aircraft 1 (2008) 1–6.
[10] K. Liang, B. Yang, Z. Zhang, Investigation of heat transfer and coking characteristics of hydrocarbon fuels, J. Propul. Power 14 (5) (1998) 789–796.
[11] D. Preclik, G. Hagemann, O. Knab, L. Brummer, C. Mading, D. Wiedmann, P. Vuillermoz, LOX/hydrocarbon propellant trade considerations for future reusable liquid booster engines, in: 41st AIAA/ASME/SAE/ASEE Joint Propulsion Conference & Exhibit, 2005, p. 3567.
[12] J.P. Stempien, M. Ni, Q. Sun, S.H. Chan, Production of sustainable methane from renewable energy and captured carbon dioxide with the use of solid oxide electrolyzer: a thermodynamic assessment, Energy 82 (2015) 714–721.
[13] T. Amon, B. Amon, V. Kryvoruchko, A. Machmüller, K. Hopfner-Sixt, V. Bodiroza, R. Hrbek, J. Friedel, E. Pötsch, H. Wagentristl, et al., Methane production through anaerobic digestion of various energy crops grown in sustainable crop rotations, Bioresource Technol. 98 (17) (2007) 3204–3212.
[14] O. Knab, M. Frey, J. Görgen, K. Quering, D. Wiedmann, C. Mäding, Progress in combustion and heat transfer modelling in rocket thrust chamber applied engineering, in: 45th AIAA/ASME/SAE/ASEE Joint Propulsion Conference & Exhibit, 2009, p. 5477.
[15] O.J. Haidn, N. Adams, R. Radespiel, W. Schröder, C. Stemmer, T. Sattelmayer, B. Weigand, Fundamental technologies for the development of future space transport system components under high thermal and mechanical loads, in: 54th AIAA/SAE/ASEE Joint Propulsion Conference, 2018, p. 4466.
[16] F. Cuoco, B. Yang, M. Oschwald, Experimental investigation of LOX/H2 and LOX/CH4 sprays and flames, in: 24th International Symposium on Space Technology and Science, 2004.
[17] J. Lux, D. Suslov, M. Bechle, M. Oschwald, O.J. Haidn, Investigation of sub-and supercritical LOX/methane injection using optical diagnostics, in: 42nd AIAA/ASME/SAE/ASEE Joint Propulsion Conference & Exhibit.
[18] M. Shim, K. Noh, W. Yoon, Flame structure of methane/oxygen shear coaxial jet with velocity ratio using high-speed imaging and OH∗, CH∗ chemiluminescence, Acta Astronaut. 147 (2018) 127–132.
[19] F. Grisch, E. Bertseva, M. Habiballah, E. Jourdanneau, F. Chaussard, R. Saint-Loup, T. Gabard, H. Berger, CARS spectroscopy of CH4 for implication of temperature measurements in supercritical LOX/CH4 combustion, Aerospace Sci. Technol. 11 (1) (2007) 48–54.
[20] D. Suslov, B. Betti, T. Aichner, S. Soller, F. Nasuti, O. Haidn, Experimental investigation and CFD-simulation of the film cooling in an O2/CH4 subscale combustion chamber, in: Space Propulsion Conference, 2012.
[21] D. Eiringhaus, H. Riedmann, O. Knab, O.J. Haidn, Full-scale virtual thrust chamber demonstrators as numerical testbeds within sfb-trr 40, in: 54th AIAA/SAE/ASEE Joint Propulsion Conference, AIAA 2018-4469, 2018, p. 4469. doi:https://doi.org/10.2514/6.2018-4469.
[22] H. Negishi, Y. Daimon, H. Kawashima, Flowfield and heat transfer characteristics in the le-x expander bleed cycle combustion chamber, in: 50th AIAA/ASME/SAE/ASEE Joint Propulsion Conference, AIAA 2014-4010, 2014, p. 4010. doi:https://doi.org/10.2514/6.2014-4010.
[23] H. Negishi, Y. Daimon, H. Kawashima, N. Yamanishi, Conjugated combustion and heat transfer modeling for full-scale regeneratively cooled thrust chambers, in: 49th AIAA/ASME/SAE/ASEE Joint Propulsion Conference, 2013, p. 3997.
[24] J. Song, B. Sun, Coupled numerical simulation of combustion and regenerative cooling in lox/methane rocket engines, Appl. Therm. Eng. 106 (2016) 762–773, https://doi.org/10.1016/j.applthermaleng.2016.05.130.
[25] Y. Daimon, H. Negishi, S. Silvestri, O. Haidn, Conjugated combustion and heat transfer simulation for a 7 element GOX/GCH4 rocket combustor, in: 2018 Joint Propulsion Conference, AIAA Paper 2018-4553, 2018, p. 4553. doi: https://doi.org/10.2514/6.2018-4553.
[26] D. Suslov, R. Arnold, O. Haidn, Investigation of film cooling efficiency in a high pressure subscale lox/h2 combustion chamber, in: 47th AIAA/ASME/SAE/ASEE Joint Propulsion Conference & Exhibit, AIAA 2011-5778, 2011, p. 5778. doi: https://doi.org/10.2514/6.2011-5778.
[27] C.M. Roth, O.J. Haidn, A. Chemnitz, T. Sattelmayer, G. Frank, H. Müller, J. Zips, R. Keller, P.M. Gerlinger, D. Maestro, et al., Numerical investigation of flow and combustion in a single element GCH4/GOx rocket combustor, in: 52nd AIAA/SAE/ASEE Joint Propulsion Conference, 2016, p. 4995.
[28] N. Perakis, D. Rahn, D. Eiringhaus, Y. Daimon, S. Zhang, S. Karl, T. Horchler, O.J. Haidn, Qualitative and quantitative comparison of RANS simulation results for a 7 element GOX/GCH4 rocket combustor, in: 54th AIAA/SAE/ASEE Joint Propulsion Conference, 2018.
[29] S. Silvestri, M.P. Celano, G. Schlieben, O.J. Haidn, Characterization of a multi-injector GOX/CH4 combustion chamber, in: 52nd AIAA/SAE/ASEE Joint Propulsion Conference, 2016, p. 4992.
[30] N. Perakis, O.J. Haidn, Inverse heat transfer method applied to capacitively cooled rocket thrust chambers, Int. J. Heat Mass Transfer 131 (2019) 150–166.
[31] E.B. Coy, Measurement of transient heat flux and surface temperature using embedded temperature sensors, J. Thermophys. Heat Transfer 24 (1) (2010) 77–84.
[32] A. Vaidyanathan, J. Gustavsson, C. Segal, One-and three-dimensional wall heat flux calculations in a O2/H2 system, J. Propul. Power 26 (1) (2010) 186–189.
[33] J. Haemisch, D. Suslov, M. Oschwald, Experimental analysis of heat transfer in cooling channels of a subscale combustion chamber at real thermal conditions for cryogenic hydrogen and methane, in: Space Propulsion Conference, 2018.
[34] Fluent, 18.0 ANSYS Fluent Theory Guide 18.0, Ansys Inc.
[35] D. Rahn, D. Eiringhaus, H. Riedmann, R. Behr, O. Haidn, Characterization of an adiabatic flamelet combustion model for gaseous CH4/O2 combustion in rocket thrust chambers, in: Space Propulsion Conference 2018, 2018.
[36] E. Artioukhine, Heat Transfer and Inverse Analysis, RTO-EN-AVT-117.

[37] R. Fletcher, Practical Methods of Optimization, John Wiley & Sons, 2013.
[38] C. Kirchberger, R. Wagner, H.-P. Kau, S. Soller, P. Martin, M. Bouchez, C. Bonzom, Prediction and analysis of heat transfer in small rocket chambers, in: 46th AIAA Aerospace Sciences meeting and Exhibit, AIAA-2008-1260, Reno (NV), USA, 2008, pp. 07–11, https://doi.org/10.2514/6.2008-1260.
[39] C.U. Kirchberger, Investigation on heat transfer in small hydrocarbon rocket combustion chambers, Ph.D. thesis, Technische Universität München, 2014.
[40] V. Gnielinski, New equations for heat and mass transfer in turbulent pipe and channel flow, Int. Chem. Eng. 16 (2) (1976) 359–368.
[41] H. Kraussold, Die Wärmeübertragung an Flüssigkeiten in Rohren bei turbulenter Strömung, For. Gebiet Ingenieurwes. A 4 (1) (1933) 39–44.
[42] E. Lemmon, M. McLinden, D. Friend, P. Linstrom, W. Mallard, NIST Chemistry WebBook, Nist Standard Reference Database Number 69, National Institute of Standards and Technology, Gaithersburg.
[43] W. Chang, X. Chu, A.F.B.S. Fareed, S. Pandey, J. Luo, B. Weigand, E. Laurien, Heat transfer prediction of supercritical water with artificial neural networks, Appl. Therm. Eng. 131 (2018) 815–824, https://doi.org/10.1016/j.applthermaleng.2017.12.063.
[44] G. Scalabrin, L. Piazza, Analysis of forced convection heat transfer to supercritical carbon dioxide inside tubes using neural networks, Int. J. Heat Mass Transfer 46 (7) (2003) 1139–1154, https://doi.org/10.1016/s0017-9310(02)00382-4.
[45] N. Perakis, D. Rahn, D. Eiringhaus, O.J. Haidn, Heat transfer and combustion simulation of a 7-element GOX/GCH4 rocket combustor, in: 2018 Joint Propulsion Conference, AIAA Paper 2018-4554, 2018, p. 4554. doi: https://doi.org/10.2514/6.2018-4554.
[46] N. Peters, Laminar diffusion flamelet models in non-premixed turbulent combustion, Prog. Energy Combust. Sci. 10 (3) (1984) 319–339, https://doi.org/10.1016/0360-1285(84)9011-X.
[47] N. Slavinskaya, M. Abbasi, J.-H. Starcke, A. Mirzayeva, O.J. Haidn, Skeletal mechanism of the methane oxidation for space propulsion applications, in: 52nd AIAA/SAE/ASEE Joint Propulsion Conference, American Institute of Aeronautics and Astronautics, AIAA Paper 2016-4781, 2016, p. 4781. doi: https://doi.org/10.2514/6.2016-4781.
[48] B.E. Launder, D.B. Spalding, Mathematical Models of Turbulence, Academic Press, 1972.
[49] F.F. Winter, N. Perakis, O.J. Haidn, Emission imaging and CFD simulation of a coaxial single-element GOX/GCH4 rocket combustor, in: 54th AIAA/SAE/ASEE Joint Propulsion Conference, 2018, p. 4764.